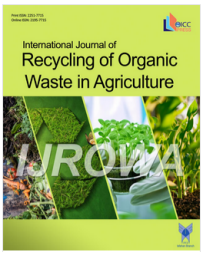

Special Issue (2024), S10 (1-17)

International Journal of Recycling Organic Waste in Agriculture (IJROWA), Special Issue

https://dx.doi.org/10.57647/ijrowa-y6fq-m572

Enhanced removal of Pb^{2+} from aqueous solutions by iron/manganese binary oxide loaded on *Eichhornia crassipes* stem biochar

Nguyen Xuan Loc[1], Tran Tan Bao[2], Phan Thi Thanh Tuyen[1], Lang Hiep Phong[2], Do Thi My Phuong[2,*]

[1]*Department of Environmental Science, College of the Environment and Natural Resources, Can Tho University, Can Tho, Vietnam.*
[2]*Department of Environmental Engineering, College of the Environment and Natural Resources, Can Tho University, Can Tho, Vietnam.*

[*]**Corresponding author:** dtmphuong@ctu.edu.vn

Original Research

Received:
30 January 2024
Revised:
5 April 2024
Accepted:
22 May 2024
Published online:
14 June 2024

Abstract:

Purpose: Biochar modified with metal oxides has proved high capacities in removing heavy metals in wastewater. There is a limited number of studies exploring the potential of Fe-Mn binary oxides-biochar adsorbents for several heavy metals removal from contaminated water; however, the adsorption behavior and mechanism for Pb^{2+} ions adsorbed on Fe-Mn binary oxide/ *Eichhornia crassipes* stem biochar composite remains unclear.

Method: In this study, *Eichhornia crassipes* stem biochar (BC) was synthesized and loaded with iron/manganese binary oxide (Fe-Mn@BC) using iron sulfate and potassium permanganate.

Results: The successful coating of Fe-Mn oxide particles on the BC surface was confirmed through EDX and FT-IR spectra. Fe-Mn@BC exhibited a specific surface area 4.34 times higher than that of BC ($S_{Fe-Mn@BC}$ = 69.636 m^2/g; S_{BC} = 16.03 m^2/g), resulting in a maximum adsorption capacity for Pb^{2+} of 1164.95 mg/g, surpassing BC's capacity of 828.84 mg/g. The optimal conditions for Pb^{2+} removal by Fe-Mn@BC were an initial Pb^{2+} concentration of 50 mg/L, an adsorbent amount of 0.01 g, an adsorption time of 60 minutes, and an adsorption temperature of 313 K. The adsorption behavior of Pb^{2+} on Fe-Mn@BC was well-described by the pseudo second-order kinetic and Freundlich models. This process involved a heterogeneous multilayer mechanism that was both spontaneous and endothermic. The adsorption mechanism comprised intra-particle diffusion and chemisorption interactions, including co-precipitation, complexation, ion exchange, and hydrogen bonding.

Conclusion: *Eichhornia crassipes* stem biochar enhanced with iron/manganese binary oxide can efficiently remove Pb^{2+} from wastewater.

Keywords: Adsorption; Biochar; *Eichhornia crassipes*; Fe/Mn binary oxide; Pb^{2+}

1. Introduction

Heavy metals persist in various elements of our environment, including soil, air, and water. Lead (Pb^{2+}), a prominent heavy metal, originates from diverse sources, and infiltrates the living systems of both humans and animals via the food chain (Raj and Das, 2023). As a result, effectively treating wastewater containing Pb^{2+} ions is crucial. A variety of techniques has been used for Pb^{2+} removal, such as membrane technology (Idress et al., 2021), ion exchange (Jokar et al., 2019), chemical precipitation (Xu et al., 2021), electrocoagulation (Sharma et al., 2020), and adsorption (Ghorbani et al., 2020). Adsorption is one of these techniques that is frequently used because of its built-in benefits, which include environmental friendliness, high efficiency, and convenience of use (Ghorbani et al., 2020). Iron and

manganese oxides, which are common in nature, offer a high specific surface area and high affinity for heavy-metal ions (Zhang et al., 2020b). These characteristics make iron and manganese oxides as efficient adsorptive materials for eliminating heavy metals such as Cd^{2+}, Pb^{2+}, Co^{2+}, and As^{3+} from wastewater (Dong et al., 2022; Park et al., 2020). Several studies demonstrated that the Fe-Mn binary oxides consist of iron mrit and manganese dioxide, thereby enhancing the ability to remove As^{3+} (Zheng et al., 2021) and Tl^{+} (Li et al., 2017). This enhancement is attributed to their physico-chemical characteristics, including an increased specific surface area, and the involvement in simultaneous redox reactions and oxyanion exchange phenomena (Sarkar et al., 2012). Notably, the amphiphilic oxides of Fe-Mn enhance the electron transfer rate and improve the oxidation process (Qiu et al., 2021). The Fe-Mn binary oxides adsorbents, however, are less stable throughout the adsorption process and can readily release Mn^{2+} into the environment, which could be harmful to human health (Yin et al., 2020). This risk of Mn^{2+} release consequently hinders the widespread application of Fe-Mn binary oxide adsorbents for water treatment. Therefore, immobilizing Fe-Mn binary oxides onto a host material is essential.

Besides Fe-Mn binary oxides, biochar - a carbon-rich derivative of charcoal - also exhibits a strong affinity for the removal of heavy metals (Akintola et al., 2020). Biochar has been recognized for its complex porous structure, oxygen-rich surface functional groups, desired pore volume and high specific surface area (Sivaranjanee et al., 2023). Biochar can be produced through the pyrolysis process of various biomass sources, including crop residues, yard waste, food waste, forestry residues, and animal manures. In recent years, biochar derived from invasive plant species has shown a high ability in removing heavy metals from wastewater. For example, the maximum adsorption capacity of ragweed (*Ambrosia artemisiifolia L.*) derived biochar produced at 450 °C was 139 mg Cd^{2+}/g and 358.7 mg Pb^{2+}/g (Lian et al., 2020); meanwhile *Bidens pilosa L.* and *Mikania micrantha* derived biochar at 500 °C exhibited adsorption capacities of 38.10 mg Cd^{2+}/g and 20.10 mg Cu^{2+}/g (Wang et al., 2021). Several studies have indicated that biochar obtained from the well-known invasive weed species, especially water hyacinth (*Eichhornia crassipes*), exhibits effective adsorption of heavy metals in wastewater. In a typical study, the stem biomass and root biomass *Eichhornia crassipes* showed maximum adsorption capacity of 77.20 mg Cd^{2+}/g and 87.20 mg Cd^{2+}/g, respectively (Wang et al., 2022b); whereas biochar-alginate capsules derived from *Eichhornia crassipes* showed a maximum adsorption capacity of 46 mg Cd^{2+}/g (Liu et al., 2020).

However, the surface of biochar usually possesses an excess of negative charges and a limited abundance of functional groups, thereby constraining its ability to adsorb heavy metals (Zhang et al., 2020a). To overcome this limitation, researchers have explored different modification methods, such as UV radiation, acid-base treatments, and the incorporation of additional functional groups (Liu et al., 2022; Peng et al., 2018). Recent studies have shown that introducing metals or metal oxides as modifications to biochar can increase the specific surface area and the presence of functional groups like hydroxyl and carboxyl groups, in that way effectively enhancing biochar's adsorption capabilities (Bao et al., 2021; Liu et al., 2021). For instance, biochar coated with zero-valent iron (Fe^{0}) demonstrated a superior Cd^{2+} adsorption capacity compared to unmodified BC, with the adsorption quantities of the modified BC exceeding those of the pristine BC by more than 2.2 times (Chen et al., 2019). Similarly, biochar modified with MgO adsorbed 18.1 mg Cd^{2+}/g, 2.8 times higher than that of unmodified biochar (Xiang et al., 2018). In another study, biochar modified with potassium permanganate ($KMnO_4$) has the capability to enhance the Cd^{2+} removal rate in aqueous solutions, demonstrating a 1.02 times improvement compared to the original biochar. This modification successfully incorporates manganese oxide particles into the biochar, resulting in the creation of micropores and an increase in the specific surface area. Consequently, more adsorption sites are made available (Li et al., 2017). Zhu et al. (2020) also mentioned that the introduced Fe particles increased Fe–OH/Fe–O, thus facilitating hydroxyl complexation and ion exchange mechanisms. As a result, the adsorption capacity of biochar modified with goethite for Cd^{2+} in water was 1.35 times higher than that of the unmodified biochar (Zhu et al., 2020). Interestingly, the combination of biochar with Fe-Mn binary oxides has been proposed as a viable solution, capitalizing on the respective strengths of both materials. In essence, biochar modified with a combination of metals demonstrates superior adsorption performance compared to biochar modified with a single metal. As an illustration, rice straw biochar modified with iron–manganese binary oxides exhibited a maximum adsorption capacity of 120.77 mg Cd^{2+}/g at 298 K. This value was notably $1.5 - 10$ times higher than the adsorption capacities observed for Cd^{2+} by potassium-modified or manganese-modified biochar (Tan et al., 2022). The efficiency of Cd^{2+} removal by biochar functionalized with Mg–Fe double hydroxides also exhibited a higher absorption capability compared to unmodified biochar, reaching up to 14.4 times that of the unmodified biochar (Tan et al., 2019).

There is a limited number of studies exploring the potential of Fe-Mn binary oxides-biochar adsorbents for As^{3+} (Lin et al., 2017), Cr^{6+} (Liang et al., 2020) and Cd^{2+} (Yin et al., 2020; Tan et al., 2022) removal from contaminated water; however, the adsorption behavior and mechanism for Pb^{2+} ions adsorbed on Fe-Mn binary oxide/ *Eichhornia crassipes* stem biochar composite remains unclear. This study aims to address this gap through batch adsorption experiments, with primary objectives including: (1) evaluating the role of Fe-Mn binary oxide loaded on pristine *Eichhornia crassipes* stem biochar in removing Pb^{2+} from aqueous solution; (2) exploring the interaction mechanisms governing the Pb^{2+} adsorption process. The investigation comprehensively explores the impacts of various operational conditions, such as solution pH, adsorbent dosage, initial Pb^{2+} concentration, contact time, and temperature. Interaction mechanisms are explored based on outcomes from adsorption kinetics, isotherm, and thermodynamic studies.

2. Material and methods

Chemicals

Iron(II) sulfate heptahydrate ($FeSO_4.7H_2O$) and potassium permanganate ($KMnO_4$) were provided from Xilong and Guangzhou Chemical Reagent Factory (China), respectively, and were analytical reagent grade (AR). Nitric acid (HNO_3), sodium hydroxide (NaOH) and hydrochloric acid (HCl) were supplied from Merck (Germany) and were guaranteed reagent grade (GR). Pb^{2+} standard stock solution of 1000 mg/L was also obtained from Merk (Germany).

Materials

The *Eichhornia crassipes* stem, from a canal in the Mekong Delta, was washed carefully, then dried at 70 °C until constant weight, and formed into cylindrical granules with a length of $2-3$ cm. The pyrolysis process of these granules took place in a furnace (Model VMF 165, Yamada Denki, Adachi, Tokyo, Japan) at 500 °C, utilizing a heating rate of 10 °C/min for a 2-hour duration in a limited oxygen environment. Following the cooling phase, the resulting biochar underwent crushing and sieving to achieve a grain size of $<$ 0.075 mm. Subsequently, the sieved biochar was subjected to washing with a solution of 0.1 M HCl and distilled water until the pH reached a range between 6.0 and 7.0. The biochar was ultimately dried overnight at 80 °C and stored for future use or further applications. These samples were specifically identified as *Eichhornia crassipes* stem biochar (BC).

The synthesis of the Fe-Mn binary oxide/*Eichhornia crassipes* stem biochar was achieved using the co-precipitation method, following a procedure with slight modifications as detailed by Tang et al. (2022). Initially, 5.0 g of biochar (BC) was measured and immersed in a combined solution containing 40 mL of 0.10 mol/L $FeSO_4$ and 40 mL of 0.25 mol/L $KMnO_4$. The mixture was stirred on a magnetic stirrer for 2 hours. This was followed by immersion in a water bath at 95 °C for 22 hours. Subsequent steps included drying and subjecting it to anaerobic pyrolysis at 300 °C for 0.5 hours. The resultant mixture was then cooled to room temperature, washed with deionized water, and ultimately dried in a dryer at 70 °C until a constant weight was achieved. The collected samples were specifically identified as Fe-Mn binary oxide/*Eichhornia crassipes* stem biochar (Fe-Mn@BC).

Adsorbent characterization

The pH and electrical conductivity (EC) of the biochar were assessed in a solution with a 1:100 ratios of biochar to deionized water, following 2 hours of agitation on a shaker (Bioshaker BR-23FH, Taitec Co., Saitama, Japan) at 100 rpm and 25 °C. The pH was determined using a pH meter (LAQUAtwin B-712, HORIBA, Japan), while the EC was measured with an EC meter (MI306, Milwaukee, Rumani). The electric furnace (AF11/6B, Lenton, Japan) was utilized to evaluate the moisture, volatile matter, and ash contents. The analysis followed a method derived from ASTM D1762-84 (2013) with minor adjustments. To elaborate, the moisture content was determined by subjecting the material to heating at 105 °C for 2 hours, the volatile matter content was analyzed in an inert atmosphere at 900 °C $\pm$ 20 °C for 7 minutes, and the ash content was assessed in an air atmosphere at 800 °C for 6 hours.

The fixed carbon content was determined using the following formula:

$$\text{Fixed carbon}(\%) = 100\% - (\text{moisture}(\%) + \text{ash}(\%) + \text{volatile matter}(\%))$$

The microstructure of adsorbents was visualized using scanning electron microscopy (SEM) (JSM-7100, JOEL Ltd., Tokyo, Japan). Additionally, energy-dispersive X-ray (EDX) spectroscopy (Hitachi, Japan) was employed to analyze the elemental surface composition of the samples. The BET-specific surface area was calculated based on the low-temperature nitrogen adsorption isotherm measured using Nova Station A (Quantachrome Instruments version 11.0, Miami, FL, USA). Functional groups on the surface samples were determined using Fourier transform infrared spectroscopy (FTIR) (FTIR-PerkinElmer Spectrum 10.5.2, Buckinghamshire, UK).

Batch adsorption studies

The stock solution containing 1000 mg/L Pb^{2+} ions was diluted with double distilled water to obtain desired concentration, in the following experiments. A measured quantity of BC and Fe-Mn@BC (0.01 g) was added into a known volume (50 mL) of a Pb^{2+} ion solution with concentrations ranging from 50 to 200 mg/L. This mixture was placed in a 125 mL Erlenmeyer flask. To establish the desired initial pH values (ranging from 2 to 10), 0.1 M HCl or 0.1 M NaOH was added. The resulting mixture was then agitated at a constant speed of 60 rpm at room temperature (298 K) for a specified duration. Subsequently, the mixture was filtered using Whatman No. 1 filter paper to separate the adsorbent from the Pb^{2+} solution. The concentration of Pb^{2+} was measured both before and after adsorption using the PinAAcle 900 T Atomic Absorption Spectrophotometer (Perkin-Elmer) in Graphite-Furnace Atomic Absorption Spectrometry (GFAAS) mode.

The adsorption capacity (q_e) and the percentage removal (%) were calculated using equations (1) and (2), respectively, as referenced from Deb et al. (2023):

$$q_e = \frac{(C_0 - C_e)\cdot V}{m} \ (\text{mg/g}) \tag{1}$$

$$H = \frac{(C_0 - C_e)\cdot 100}{C_0} \ (\%) \tag{2}$$

where C_0 and C_e (mg/L) are the initial Pb^{2+} concentration and Pb^{2+} concentration at equilibrium, m (g) is the weight of the BC or Fe-Mn@BC adsorbents, and V (L) is the volume of Pb^{2+} solution.

The adsorption equilibrium data for Pb^{2+} onto BC or Fe-Mn@BC were examined using the linear forms of three two-parameter kinetic and isotherm models. The models were initially applied with the experimental values of q_e and C_e to determine the parameters of the equations. The linearized equations for kinetic models and isotherm models are detailed in Table SM1 and Table SM2, respectively.

Error analysis

Two distinct error functions, namely Chi-square (χ^2) and the coefficient of determination (R^2), were utilized to identify the appropriate isotherm and kinetic models for representing the experimental data. These parameters were determined by minimizing the corresponding error functions through the use of the Solver add-in Excel. The expressions for the calculated error functions are presented in equations (3) to (4) below, as referenced from Bopda et al. (2019).

$$\chi^2 = \sum_{i=1}^{n} \frac{(q_{e,\text{exp}} - q_{e,\text{cal}})^2}{q_{e,\text{cal}}} \quad (3)$$

$$R^2 = \frac{(q_{e,\text{exp}} - \bar{q}_{e,\text{cal}})^2}{\sum_{i=1}^{n}(q_{e,\text{exp}} - \bar{q}_{e,\text{cal}})^2 + (q_{e,\text{exp}} - q_{e,\text{cal}})^2} \quad (4)$$

3. Results and discussion

Characterization

Physicochemical properties

The values of pH, EC, fixed C, and ash of BC and Fe-Mn@BC are shown in Table 1. The Fe-Mn@BC exhibited higher ash content (40.74%) but lower pH (8.90), EC (1368.56 µS/cm), and fixed C (24.38%) compared to their respective pristine BC. This difference was attributed to the incorporation of Fe-Mn binary oxide. Consistent with earlier research, the contrasting patterns observed between pH and ash content could be attributed to the buildup of cations and carbonates on the BC and Fe-Mn@BC (Qu et al., 2023). The iron (Fe) present in Fe-Mn@BC underwent a reaction with OH^-, leading to the formation of FeOH and $FeOH_2^+$ groups, thereby causing a decrease in pH (Sadegh-Zadeh and Seh-Bardan, 2013). A negative correlation between fixed C and ash content was observed, suggesting that Fe-Mn@BC with elevated ash content exhibited lower fixed C levels compared to its precursor BC (Nguyen et al., 2018).

Table 1. Physicochemical properties of pristine BC and Fe-Mn@BC.

Parameter[a]		BC	Fe-Mn@BC
pH		9.66	8.90
pH_{pzc}		6.97	6.05
EC (µS/cm)		3376.67	1368.56
Fixed C (%)		26.68	24.38
Ash content (%)		36.76	40.74
BET analysis	S_{BET} (m^2/g)	16.03	69.64
	V_{pore} (cm^3/g)	0.017	0.059
	D_P (nm)	2.50	2.08

[a]Values are the average of triplicates.

Textural properties

The textural properties, including specific surface area, average pore size, and pore volume, were determined using established calculation methods such as the Brunauer–Emmett–Teller (BET) and the Barrett–Joyner–Halenda (BJH) models. Fig. 1 A displays the nitrogen adsorption–desorption curves for BC and Fe-Mn@BC, while Fig. 1 B illustrates the pore size distributions estimated by the BJH method from desorption branches.

Under low relative pressure conditions ($P/P_0 \leq 0.1$), both BC and Fe-Mn@BC isotherms display a characteristic type I behavior. This indicates a linear increase in nitrogen adsorption as the relative pressure rises, pointing to the existence of micropores. In the medium relative pressure range ($0.5 < P/P_0 < 0.9$), a nearly closed hysteresis loop forms, and the isotherms exhibit the type IV characteristic, suggesting the presence of mesopores (Fang et al., 2020). The desorption curves of BC and Fe-Mn@BC closely align with their adsorption curves, exhibiting variations primarily at mid to high P/P_0. Following the International Union of Pure and Applied Chemistry (IUPAC) classification, the nitrogen adsorption–desorption isotherms for BC and Fe-Mn@BC fall into type IV shapes with type H4 hysteresis loops, indicating the presence of slit-shaped pores associated with

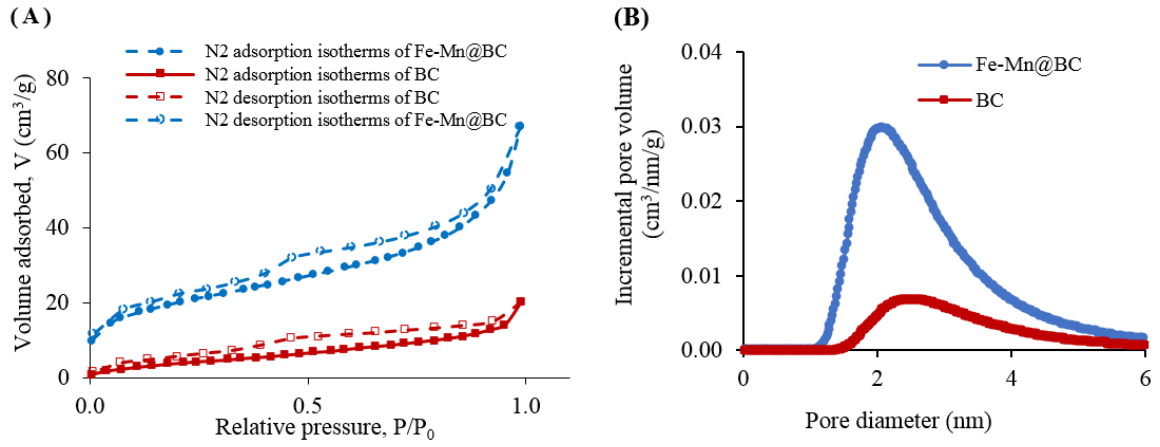

Figure 1. (A) Nitrogen adsorption-desorption isotherms at 77 K of BC and Fe-Mn@BC; (B) Pore size distribution of BC and Fe-Mn@BC.

mesoporosity (Dwivedi et al., 2022). This conclusion is further supported by the corresponding pore size distribution depicted in Fig. 1 B. Both prepared BC and Fe-Mn@BC surfaces exhibit mesoporosity, with mean pore radii of approximately 2.50 nm and 2.08 nm, respectively.

As illustrated in Figs. 1 A and 1 B, the Fe-Mn@BC demonstrates a superior nitrogen adsorption compared to the BC, indicating enhanced specific surface area and pore volume for Fe-Mn@BC (Table 1). Specifically, the BET-calculated specific surface area (S_{BET}) for Fe-Mn@BC was 69.64 m^2/g, surpassing BC's 16.03 m^2/g. The pore volume of Fe-Mn@BC increased to 0.059 cm^3/g, contrasting with BC's 0.017 cm^3/g. These findings align with the study by Tang et al. (2022), where the conversion of straw material into Fe-Mn@BC resulted in a significantly higher specific surface area of 13.726 m^2/g compared to BC's 0.754 m^2/g. Also, the pore volume increased from 0.0002 cm^3/g (BC) to 0.003 cm^3/g (Fe-Mn@BC). This phenomenon can be ascribed to the creation of new pores occurring during the modification process, resulting in an expanded specific surface area. Several studies have demonstrated that adsorbent materials with higher specific surface areas possess more functional groups and are more flexible in exchange reactions, thereby enhancing the adsorption of Pb^{2+} ions (Fan et al., 2020; Benettayeb et al., 2022). Generally, the average pore sizes of pristine BC and Fe-Mn@BC were 2.50 nm and 2.08 nm, respectively. This suggests the incorporation of Fe-Mn binary oxide particles onto the *Eichhornia crassipes* stem biochar, leading to the occupation of certain pore spaces.

FTIR spectra

Functional groups on both BC and Fe-Mn@BC were identified through FT-IR analysis. As depicted in Fig. 2, the FT-IR spectra of Fe-Mn@BC exhibited some distinctions from those of BC. Specifically, the FT-IR spectra of BC in this investigation closely resembled those of other high-temperature biochars derived from *Eichhornia crassipes* (Hashem et al., 2020; Narayanan et al., 2021). In particular, the presence of two peaks around 3413 cm^{-1} and 1581 cm^{-1} was attributed to the vibration of -OH and the stretching vibration of aromatic C=C/C=O double bonds, respectively (Qu et al., 2023). These functional groups serve as active sites for binding Pb^{2+}. Furthermore, the peak associated with the stretching vibration of C=O and O-C-O was identified at around 1423 and 1036 cm^{-1}, respectively (Yin et al., 2020).

In Fig. 2, notable differences were observed in the FT-IR spectrum of Fe-Mn@BC, specifically alterations in signal intensities at 1423 cm^{-1} and 874 cm^{-1}. The vibrational band within the range of 1420 – 1475 cm^{-1} indicates C=O bond vibrations in pure $CaCO_3$ (Chen and Nan, 2011). Consequently, the broad peak at 1423 cm^{-1} encompasses vibrations of C=O bonds in the carbonate anion (CO_3^{2-}) (Hospodarova et al., 2018). Additionally, the relatively strong intensity peaks at 874 cm^{-1} are associated with C=O bonds in the carbonate anion (Hospodarova et al., 2018).

In general, in comparison to the pristine *Eichhornia crassipes* stem BC, the bands in the Fe-Mn@BC were more intense and broader, suggesting that Fe-Mn@BC has a greater abundance of functional groups and an improved capability for Pb^{2+} adsorption. The presence of a peak at approximately 564 cm^{-1} in the Fe-Mn@BC spectra was attributed to the vibration of Fe-O/Mn-O (Wang et al., 2018; Zhou et al., 2018), providing evidence for the successful loading of Fe/Mn oxide onto the *Eichhornia crassipes* stem biochar.

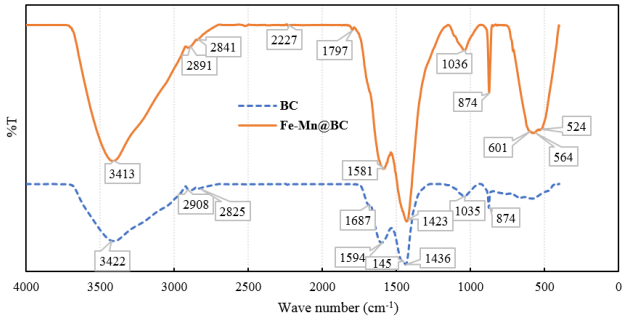

Figure 2. The FT-IR spectra of BC and Fe-Mn@BC.

(A)

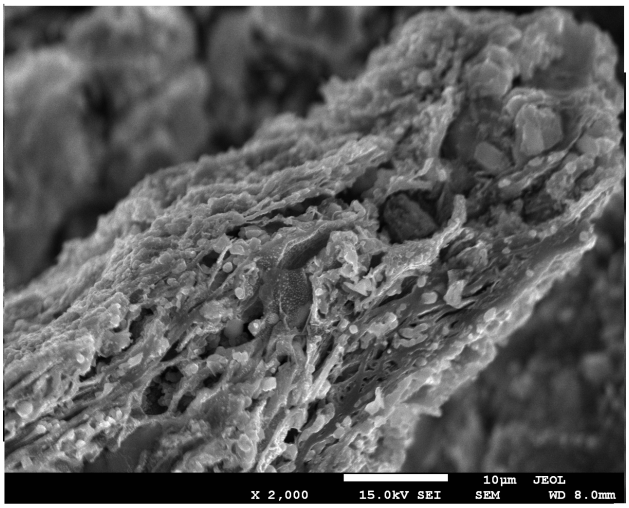

(B)

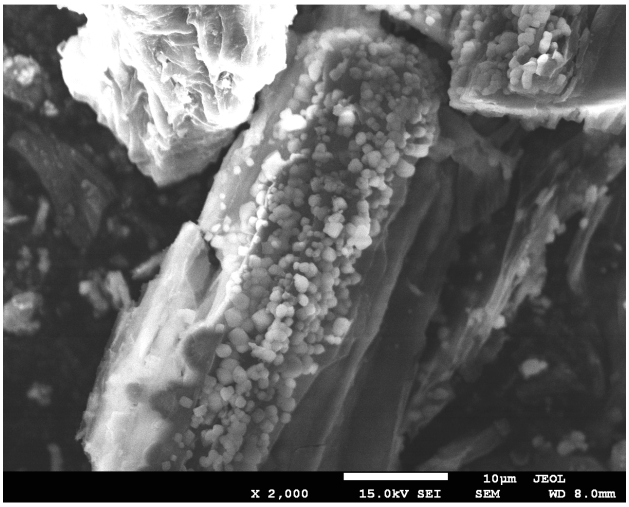

Figure 3. The SEM images of (A) BC, and (B) Fe-Mn@BC.

SEM investigation

The surface morphology of the synthesized BC and Fe-Mn@BC was analyzed using a magnification of 2000x and an acceleration voltage of 15 kV. The obtained SEM images, depicted in the Fig. 3, displayed a long fiber structure on the surface of biochar, consistent with prior observations for biochar derived from *Eichhornia crassipes* stem (Carneiro et al., 2023; Zhou et al., 2019).

Fig. 3 A depicts the morphological structure of the biochar, exhibiting a smooth surface and uniform pore structure. Conversely, impregnation with iron and manganese salts led to surface corrosion, disruption of the biochar's pore structures, and the aggregation of numerous particles, as illustrated in Fig. 3 B. Based on the EDX analysis below, these particles have been identified as iron and manganese oxides.

EDX spectra

The EDX spectrum illustrated the prominent presence of carbon (C), oxygen (O), and chlorine (Cl), along with minor elements phosphorus (P), magnesium (Mg), potassium (K), and calcium (Ca) in the BC derived from *Eichhornia crassipes* stem, as depicted in Fig. 4 A. The iron/manganese binary oxide loaded on *Eichhornia crassipes* stem biochar (Fe-Mn@BC) was confirmed by the EDX spectrum in Fig. 4 B, which exhibited similar peaks compared to the original BC. Notably, the presence of metal ions such as iron (Fe) and manganese (Mn) was distinctly evident in the EDX spectrum following the modification. Specifically, peaks at approximately 0.57, 5.85, and 6.4 keV acceleration voltage corresponded to Mn ion, while the narrow peaks around 0.62 and 6.1 keV acceleration voltage were attributed to Fe ion. This observation confirmed the appearance of Mn and Fe peaks in the Fe-Mn@BC sample.

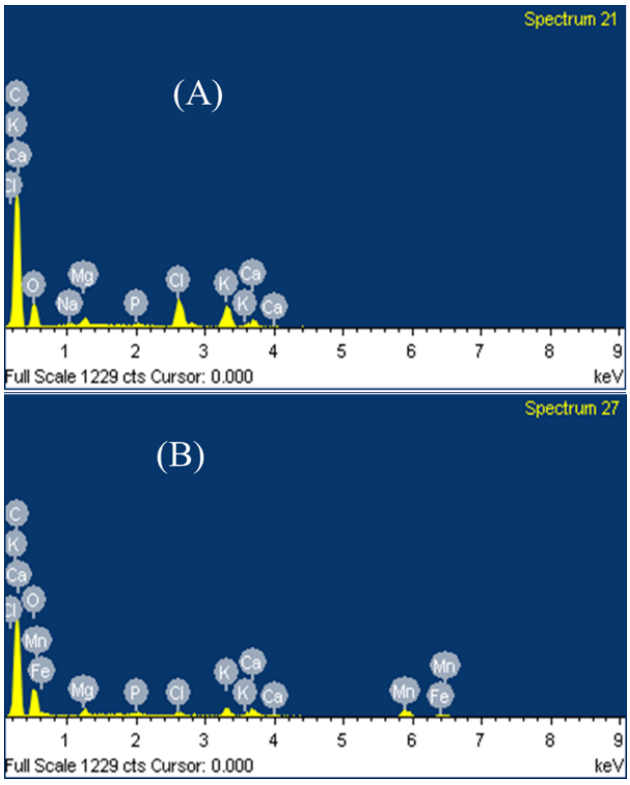

Figure 4. EDX spectrum of (A) BC, and (B) Fe-Mn@BC.

Drawing conclusions from the FT-IR and EDX findings, it can be affirmed that Fe-Mn binary oxide has been effectively bonded with the *Eichhornia crassipes* stem biochar matrix. Exploiting the physical attributes of BC and Fe-Mn@BC, an evaluation was conducted to test the feasibility of Pb^{2+} removal, with the results detailed in the subsequent section.

Pb^{2+} adsorption tests

Effect of pH

The surface charge density of the adsorbents and the predominant state of Pb^{2+} can be affected by the pH level. The data obtained regarding the adsorption of Pb^{2+} ions by BC and Fe-Mn@BC, with a pH range of $2-10$ and an initial Pb^{2+} ion concentration of 50 mg/L, is illustrated in Fig. 5 A. The adsorption process exhibited a high dependence on pH, with removal efficiency continuously increasing as the initial pH rose. The removal of Pb^{2+} experienced an increase when the pH value increased from 2 to 10 for both BC and Fe-Mn@BC. Particularly, the adsorption capacity of BC for Pb^{2+} ions rose from 46.27 to 51.47 mg/g, while for Fe-Mn@BC, it increased from 51.45 to 54.41 mg/g. The percentage removal also exhibited an increase from 87.89% to 99.93% for BC and from 97.72% to 99.95% for Fe-Mn@BC, with the increase in pH from 2 to 10.

The adsorption capacities of Pb^{2+} by both BC and Fe-Mn@BC were noticeably reduced under low–pH conditions (pH 2 and 4). At a starting pH of 2.0, the BC and Fe-Mn@BC demonstrated a limited removal rate because of the competition between Pb^{2+} and H_3O^+ for surface adsorption sites (Tran et al., 2017; Yin et al., 2020). Simultaneously, MnO_x and FeO_x supported on Fe-Mn@BC could dissolve into the solution as free ions at low pH, resulting in a depletion of potential adsorption capacity for Pb^{2+} (Qiu et al., 2019; Yin et al., 2020).

Besides, the pH at the point of zero charge (pH_{pzc}) can be utilized to explain the adsorption trend of BC and Fe-Mn@BC. In this study, the pH_{pzc} of the samples was determined through pH drift tests, following the procedure described by Loc et al. (2023). The pH_{pzc} values of both BC and Fe-Mn@BC are provided in Table 1, with BC having a pH_{pzc} of 6.97 and Fe-Mn@BC having a pH_{pzc} of 6.05. When the environmental pH is below the pH_{pzc} value, the surface charge of the material becomes positive, resulting in both BC and Fe-Mn@BC exhibiting positive surfaces under these conditions. However, these positive surface charges do not promote the adsorption of Pb^{2+} by either BC or Fe-Mn@BC due to electrostatic repulsion. Consequently, the adsorption capacity of BC and Fe-Mn@BC at pH 2 and 4 was lower compared to pH levels of 6, 8, and 10.

Another possible reason, the solution's pH was noted to impact the chemical status of lead. At low pH levels, only Pb^{2+} was identifiable. With increasing pH, the solution's alkalinity induced hydrolysis, giving rise to $Pb(OH)^+$ and ultimately causing the precipitation of $Pb(OH)_2$ (Do and Lee, 2013). As the pH increases, the positive charge on the

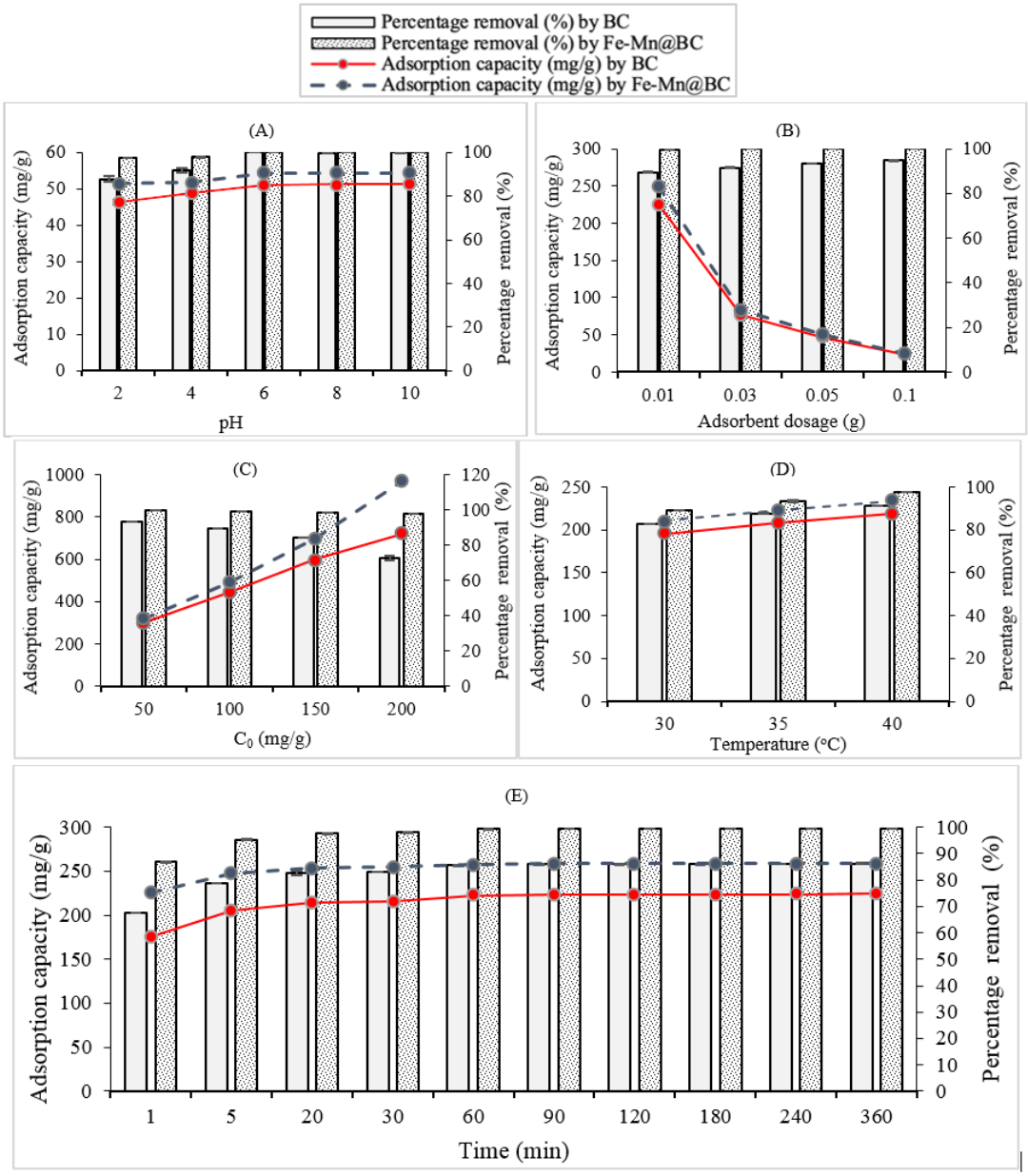

Figure 5. Effect of pH (A), adsorbent dosage (B), initial Pb^{2+} concentration (C), temperature (D), and adsorption time (D) on adsorption capacity and percentage removal of Pb^{2+} ions onto BC and Fe-Mn@BC.

surfaces of BC and Fe-Mn@BC gradually diminishes. This reduction leads to a decrease in the repulsive force between BC or Fe-Mn@BC and Pb^{2+}, contributing to an increase in adsorption capacity. With further pH elevation, the surface electrical properties shift from positive to negative, transforming the repulsive force into an attractive force, thereby favoring Pb^{2+} adsorption. This process reached a peak removal rate of Pb^{2+} at 99.9% when the pH exceeds 6.

It's worth noting that at pH = 6, both BC and Fe-Mn@BC demonstrated adsorption capacity and efficiency values comparable to the highest observed. Beyond this pH level, both adsorption capacity experienced insignificant changes. Furthermore, the removal rates of Pb^{2+} showed no apparent changes within the pH range of 6 to 10 for both BC and Fe-Mn@BC. This stability can be attributed to the deprotonation of hydroxyl and carboxyl groups, reaching saturation in their adsorption capacity (Liang et al., 2017). This indicates that a high pH condition is not necessarily required during the Pb^{2+} adsorption process on BC and Fe-Mn@BC. Consequently, a pH of 6 was identified as the optimal condition for effectively removing Pb^{2+} from aqueous solutions, consistent with findings reported in published articles on various adsorbents (Wang et al., 2022a).

Effect of adsorbent dosage

The impact of Fe-Mn@BC and BC dosages on Pb^{2+} adsorption in water is depicted in Fig. 5 B. It is evident that as the Fe-Mn@BC and BC dosages increased from 1 to 10 g/L, the adsorption capacity of Pb^{2+} decreased, while the removal efficiency increased within the $1-10$ g/L range. Specifically, the Pb^{2+} adsorption capacity gradually decreased from 250.22 to 25.13 mg/g for Fe-Mn@BC and

from 225.03 to 23.79 mg/g for BC as the dosages increased. However, the removal rate of Pb^{2+} ions increased with the rise in the adsorbent dosage. For Fe-Mn@BC, the removal rate of Pb^{2+} increased from 99.57 to 99.99%, and for BC, it increased from 89.54% to 94.69%.

This trend can be explained as follows: with an increase in Fe-Mn@BC and BC dosage, the number of available adsorption sites increases, leading to an increase in the percent removal of Pb^{2+} (Saha et al., 2023a). However, the high dosage of Fe-Mn@BC and BC can lead to particle interactions, such as the aggregation of adsorption sites. This aggregation may result in a decrease in the total biochar surface area available for Pb^{2+} adsorption and an increase in diffusion path length (Phuong et al., 2019). Consequently, the amount of Pb^{2+} (mg) absorbed per gram of Fe-Mn@BC and BC decreases with increasing Fe-Mn@BC and BC dosage.

Effect of initial Pb^{2+} concentration

The impact of various initial Pb^{2+} concentrations, ranging from 50 to 200 mg/L, is evaluated and presented in Fig. 5 C. As the initial Pb^{2+} concentration increased, the amount of Pb^{2+} adsorbed per unit mass of Fe-Mn@BC and BC (q_e) rapidly increased. For BC, q_e rises from 297.96 to 720.57 mg/g, while for Fe-Mn@BC, it increases from 317.61 to 971.61 mg/g. This rapid increase is attributed to the high number of unoccupied adsorption sites on the Fe-Mn@BC and BC surfaces, providing a greater chance for Pb^{2+} adsorption (Saha et al., 2023a). However, when the Pb^{2+} concentration in the solution increases, the available adsorption sites in the Fe-Mn@BC and BC become more quickly saturated, resulting in a reduction in the removal efficiency of Pb^{2+}. For BC, the removal efficiency decreased from 93.50% to 72.76%, while for Fe-Mn@BC, it decreased from 99.67% to 98.10%.

Effect of temperature

A temperature range of $30-40$ °C ($303-313$ K) was utilized to investigate the impact of temperature on Pb^{2+} adsorption. As shown in Fig. 5 D, the amount of Pb^{2+} adsorbed on Fe-Mn@BC and BC demonstrated a slight increase with rising temperature, with values escalating from 195.44 to 218.78 mg/g for BC and from 210.40 to 233.54 mg/g for Fe-Mn@BC. The rising adsorption capacity of Fe-Mn@BC and BC for Pb^{2+} suggests an endothermic adsorption process. This increase can be attributed to several factors. Firstly, increasing temperature may trigger swelling effects within the internal structure of Fe-Mn@BC and BC, facilitating deeper penetration of Pb^{2+} molecules into their smaller pores. Additionally, as temperature increases, the diffusion rate of Pb^{2+} molecules across the external boundary layer and into the internal pores of Fe-Mn@BC and BC particles may accelerate, leading to higher adsorption capacities. These combined mechanisms contribute to the observed enhancement in Pb^{2+} adsorption at higher temperatures (Phuong et al., 2019).

Effect of adsorption time

The effect of adsorption time was investigated to understand its influence on the adsorption efficiency of Pb^{2+} onto BC and Fe-Mn@BC. It was observed from Fig. 5 E that initially, within 20 minutes of contact time, there was a rapid increase in Pb^{2+} adsorption due to the abundance of available adsorption sites on BC and Fe-Mn@BC (Saha et al., 2023a). Subsequently, as the contact time increased, the removal efficiency of Pb^{2+} continued to gradually increase until reaching adsorption equilibrium at 60 minutes. Beyond this point, further increases in contact time did not significantly enhance Pb^{2+} adsorption, indicating that the process had reached its maximum capacity. This behaviour suggests that the duration of contact time plays a crucial role in determining the efficiency of Pb^{2+} adsorption onto BC and Fe-Mn@BC.

Adsorption kinetics

To understand the mechanisms governing the adsorption of Pb^{2+} by BC and Fe-Mn@BC, the kinetic experimental data underwent examination using three kinetic models: The Pseudo-second-order, Elovich, and Intra-particle diffusion. The equations expressing these kinetic models are shown in Table SM1 (Saleh, 2022). The graphical representations of these models can be observed in Figs SM1 and SM2, and their respective linear kinetic parameters are detailed in Table 2.

Table 2. Regression parameters of Pb^{2+} adsorption kinetics and Pb^{2+} adsorption isotherm.

	Kinetics											
	Pseudo second-order					***Elovich***				***Intra-particle diffusion***		
	$q_{e,\exp}$	$q_{e,\mathrm{cal}}$	k_2	χ^2	R^2	β	α	χ^2	R^2	k_p	C	χ^2
	mg/g	mg/g	g/mg.min			g/mg	mg/g.min			mg/g.min$^{1/2}$	mg/g	
BC	215.22	224.78	0.01	1.59	0.93	0.13	2.55×10^{11}	2.48	0.86	1.90	198.29	4.84
Fe-Mn@BC	253.39	259.08	0.01	1.25	0.96	0.20	1.34×10^{21}	3.77	0.80	1.19	242.76	2.07
	Isotherms											
	Langmuir					***Freundlich***				***Temkin***		
	q_m	K_L	χ^2	R^2	1/n	K_F	χ^2	R^2	b	K_T	χ^2	R^2
	mg/g	L/mg				(mg/kg)/(mg/L)^n			J/mol	1/mg		
BC	828.84	0.12	21.84	0.92	0.35	190.70	5.86	0.97	14.75	1.44	0.52	0.99
Fe-Mn@BC	1164.95	1.14	51.44	0.93	0.39	568.02	2.26	0.99	11.05	15.70	24.56	0.95

Analysis of the two linear error functions in Table 2 showed that the χ^2 values for the pseudo second-order kinetic model were the smallest, and its linear regression coefficient R^2 value were the highest for Pb^{2+}. The calculated equilibrium adsorption capacities ($q_{e,\text{cal}}$) obtained through the pseudo second-order kinetics model were also found to be in good agreement with the experimental equilibrium adsorption capacities ($q_{e,\text{exp}}$). These findings signify an agreement of the adsorption data with the pseudo second-order kinetic model. The pseudo-second-order kinetic model assumes that the rate-limiting step involves chemical sorption or chemisorption. It provides predictions across the entire adsorption range, with the adsorption rate primarily dependent on the adsorption capacity rather than the concentration of the adsorbate (Nasser et al., 2024). Therefore, based on the successful fitting of the adsorption data with the pseudo second-order kinetic model, it suggests that the adsorption mechanism is primarily governed by chemisorption. This process entails electrostatic attraction between Pb^{2+} ions and either BC or Fe-Mn@BC. This conclusion is in line with earlier research findings regarding the impact of solution pH on the adsorption process (Hashem et al., 2020; Tang et al., 2022).

The intraparticle diffusion model, introduced by Weber and Morris, has found widespread application in analyzing adsorption kinetics. This model accounts for three main mass transfer processes: external diffusion (or film diffusion), which involves the transfer of adsorbate in the liquid film surrounding the adsorbent; internal diffusion (or intraparticle diffusion), which pertains to the transfer of adsorbate within the pores of the adsorbent; and adsorption onto the active sites (Wang and Guo, 2022). The adsorption kinetics data of BC and Fe-Mn@BC fitted to the intraparticle diffusion model are illustrated in Fig. SM2, accompanied by their respective parameter values in Table SM3. From Fig. SM2, it is evident that the graphs of q_t versus $t^{1/2}$ for the intra-particle diffusion models of Pb^{2+} adsorption onto BC and Fe-Mn@BC showed three similar, interdependent linear lines. This observation suggests the occurrence of three stages during the adsorption process. In the initial linear stage (Stage I: $t = 1-20$ min), external diffusion or liquid film diffusion was observed, marked by the rapid uptake of Pb^{2+} ions. During this stage, Pb^{2+} ions were transported from the bulk liquid phase to the external surface of BC and Fe-Mn@BC through a liquid boundary layer. Following this, there was an intermediate stage (Stage II: $t = 30-90$ min), characterized by a more gradual uptake. This slowdown was attributed to the intra-particle pore diffusion of Pb^{2+} ions, migrating from the external surfaces of BC and Fe-Mn@BC into the macropores, mesopores, and micropores within BC and Fe-Mn@BC. The progression continued until reaching the final plateau (Stage III: $t > 90$ min), indicating the establishment of adsorption equilibrium. During this stage, intra-particle diffusion started to slow down due to a decreased Pb^{2+} concentration in the solution, coupled with a reduction in available adsorptive sites on the BC and Fe-Mn@BC.

The results from Table SM3 also suggest that the regression curves consistently exhibited straight-line patterns, indicating a relatively strong correlation ($R^2 = 0.77-0.99$). This observation points to a significant impact of the porous diffusion mechanism on the adsorption process of Pb^{2+}/BC or Pb^{2+}/Fe-Mn@BC. Noteworthy is the finding that the rate constant for the initial stage (kp_1) was 5 times higher for BC and 8 times higher for Fe-Mn@BC compared to that of the second phase (kp_2). Additionally, it was 93 times higher for BC and 147 times higher for Fe-Mn@BC than the final stage (kp_3) for Pb^{2+}. This difference indicates that the resistance to diffusion in the boundary layer was significantly less than that in the pore diffusion steps.

Adsorption isotherms

In this study, the equilibrium data were subjected to modelling using the linearized Langmuir, Freundlich, and Temkin isotherms to forecast the adsorption capacity of BC and Fe-Mn@BC for Pb^{2+} in wastewater. The equations expressing the Langmuir, Freundlich and Temkin isotherm models are shown in Table SM2 (Saha et al., 2023b). The linear fitting of Langmuir, Freundlich, and Temkin isotherms is illustrated in Fig. SM3, and their respective parameters are summarized in Table 2.

Upon a thorough analysis of the error functions in Table 2, it is apparent that, in the case of BC material, the Temkin model displayed the smallest χ^2 values and the highest R^2 values. These findings confirm that the Temkin model effectively describes the isotherms of the Pb^{2+} adsorption process by BC. The positive change in adsorption energy, denoted as b (14.75 kJ/mol), indicates that the adsorption of Pb^{2+} onto BC is an exothermic reaction. It is widely recognized that physical adsorption typically exhibits adsorption energy within the range of $5-40$ kJ/mol (Koyuncu and Okur, 2021), suggesting the possibility of physisorption mechanism due to weak Van der Waals forces between Pb^{2+} and BC (Goswami et al., 2024).

Regarding Fe-Mn@BC, the Freundlich model displayed the smallest χ^2 values and the highest R^2 values (Table 2). These findings confirm that the Freundlich model effectively describes the isotherms of the Pb^{2+} adsorption process by Fe-Mn@BC, assuming that adsorption takes place on a heterogeneous surface with a nonuniform distribution of heat of adsorption over the surface. Furthermore, the 1/n values fell within the $0-1$ range, suggesting saturation of active sites as the initial concentrations of Pb^{2+} increased. The adsorption process in this system could be characterized as favorable chemisorption on a heterogeneous surface (Tan et al., 2016).

The calculated K_F constant is closely linked to the characteristics of the adsorbent, adsorbate, and temperature. Notably, the K_F values for Fe-Mn@BC (568.02 (mg/kg)/(mg/L)^n surpass those for BC (190.70 (mg/kg)/(mg/L)^n, indicating a heightened affinity and intensity of Fe-Mn@BC for Pb^{2+} compared to pristine BC. Furthermore, the 1/n values associated with each absorbent were observed to between $0-1$ range. This observation indicates saturation of the active sites as the initial concentrations of Pb^{2+} increased. The adsorption mechanism in this system therefore can be described as advantageous chemisorption taking place on the heterogeneous surface (Tan et al., 2016).

Adsorption thermodynamics

The spontaneity of a reaction was evaluated by analyzing thermodynamic parameters, including Gibbs free energy ΔG (J/mol), enthalpy ΔH (J/mol), and entropy ΔS (J/mol.K). The thermodynamic features of Pb^{2+} adsorption onto BC and Fe-Mn@BC were investigated under conditions of pH 6.0 and temperatures of 303, 308 and 313 K, maintaining a concentration of 50 mg/L. These values were determined using equations (5) to (7), as cited in Tan et al. (2016).

$$\ln \mathrm{K}_d = \frac{\Delta S}{R} - \frac{\Delta H}{RT} \tag{5}$$

$$\Delta G = \Delta H - T\Delta S \tag{6}$$

$$\mathrm{K}_d = \frac{q_e}{C_e} \tag{7}$$

Here, R represents the universal gas constant (8.314 J/mol.K), and T denotes the absolute temperature in Kelvin. By graphing $\ln \mathrm{K}_d$ against $1/T$, one can derive ΔH and ΔS values from the slope and intercept, respectively.

The resulting thermodynamic parameters are presented in Table SM4, illustrating that negative ΔG values were observed for both BC and Fe-Mn@BC adsorbents. This suggests that, under the experimental conditions, the adsorption of Pb^{2+} was thermodynamically favorable and spontaneous (Phuong et al., 2019). The data reveals that as the temperature rose from 303 to 313 K, the ΔG values decreased by 22.4% and 31.8% for the adsorption of Pb^{2+} by BC and Fe-Mn@BC, respectively. This signifies an enhanced spontaneity in the Pb^{2+} adsorption systems, resulting in greater removal efficiency at higher temperatures. Additionally, the ΔG values resulting from the adsorption of Pb^{2+} by BC consistently exhibited reductions of 1.33, 1.76, and 3.37 kJ/mol at temperatures of 303, 308, and 313 K, respectively, in comparison to the ΔG values acquired from Pb^{2+} adsorption by Fe-Mn@BC. This confirms that the adsorption of Pb^{2+} on Fe-Mn@BC was more spontaneous and preferred compared to BC, explaining the increased adsorption capacities observed in the isotherm study of Pb^{2+} adsorption.

The positive ΔH values indicate the endothermic nature of the Pb^{2+} adsorption process on BC and Fe-Mn@BC. This endothermic behavior involves the absorption of heat from the surroundings during the adsorption process. In general, physisorption is recognized to take place when the ΔH value is less than 40 kJ/mol, while chemisorption is assumed to occur in the range of 50 to 200 kJ/mol (Liu et al., 2020b). In this current study, the high ΔH values observed ($\Delta H_{\mathrm{BC}} = 62.05$ kJ/mol; and $\Delta H_{\mathrm{Fe-Mn@BC}} = 122.30$ kJ/mol) indicate that chemical interactions significantly impact the adsorption rate. The ΔS values were also positive ($\Delta S_{\mathrm{BC}} = 0.231$ kJ/mol. K; and $\Delta S_{\mathrm{Fe-Mn@BC}} = 0.434$ kJ/mol.K), indicating an elevated level of randomness on the BC and Fe-Mn@BC surfaces as Pb^{2+} ions were absorbed. In summary, the ΔG and ΔH values indicate the spontaneous and endothermic characteristics of the adsorption process, in line with previously reported findings (Zhang et al., 2019; Tang et al., 2022).

Performance evaluation

Table 3 presents a comparison of the adsorption performance between metal-modified biochar for Pb^{2+} removal. The results underscore the notable advantages of the developed Fe-Mn@BC composite in effectively eliminating Pb^{2+} from aqueous solutions. The Langmuir isothermal model fitting reveals a maximum adsorption capacity (q_m)

Table 3. Regression parameters of Pb^{2+} adsorption kinetics and Pb^{2+} adsorption isotherm.

Adsorbent	Equilibrium contact time (min)	Optimum pH	S_{BET} (m^2/g)	q_m (mg/g)	Mechanism	Reference
$CuFe_2O_4$@Corncob biochar	40	5.0	74.98	132.10	Inner surface complexes	Zhao et al. (2020)
Fe-Mn binary oxides@ Rice straw biochar	60	4.0	13.728	165.88	Electrostatic adsorption, chemical precipitation, complexation, ion exchange, and the transformation of Mn_2O_3 into MnO_2	Tang et al. (2022)
Fe-Mn binary oxides@ Corn straw biochar	300	4.0	323.601	113.72	Chemical interactions through the monolayer	Zhang et al. (2019)
Fe-Mn binary oxides@ Waste tea leaves biochar	30	7.0	24.38	25	Ion exchange and surface complexation	Suwunwong et al. (2021)
Sludge-derived biochar by K_2FeO_4 conditioning	120	3.0	6.87	36.1	Ion exchange with Ca^{2+} and Mg^{2+}; surface complexation of free COOH and OH; and chemical precipitation or possible physical adsorption.	Wang et al. (2021a)
$KMnO_4$-modified Bamboo biochar	60	6.0	-	123.47	Mineral precipitation, functional group complexation, ion exchange and cation–π interactions	Deng et al. (2022)
MnO_2-loaded magnetic Palm kernel cake residue biochar	30	7.0	89.38	46.64	Two steps of intra-particle diffusion	Maneechakr and Mongkollertlop (2020)
Fe-Mn binary oxides@ *Eichhornia crassipes* stem biochar	60	6.0	69.64	1164.95	Chemisorption through electrostatic attraction; chemisorption on a heterogeneous surface; intra-particle diffusion	This study

for Pb^{2+} of 1164.95 mg/g, significantly surpassing values reported for similar composites such as Fe/Mn binary oxide impregnated rice straw biochar (165.88 mg/g) (Tang et al., 2022), corn straw biochar (113.72 mg/g) (Zhang et al., 2019), and waste tea leaves biochar (25 mg/g) (Suwunwong et al., 2021). These results demonstrate the substantial application potential of iron/manganese binary oxide loaded on *Eichhornia crassipes* stem biochar in effectively removing Pb^{2+} from wastewater.

Adsorption mechanism of Pb2+ by Fe-Mn@BC

The FTIR analysis (Fig. 1) suggests the potential engagement of different groups, including O-C-O, -OH, and C=C bonds on the Fe-Mn@BC surface, in the adsorption process. Additionally, the notable enhancement in the intensity peak of CO_3^{2-} compared to its pristine BC counterpart, as indicated by the FTIR analysis, implies that chemical precipitation and complexation may be the primary processes during Pb^{2+} adsorption by Fe-Mn@BC. Another conceivable mechanism involves the formation of Pb-O and COO-Pb complexes, achieved through the complexation of Pb^{2+} with ionized oxygen functional groups (-OH or -COO) or C=C (π-electron) bonds, as documented by Chen and Qiu (2021). Additionally, Pb^{2+} could be adsorbed through an ion-exchange mechanism, as proposed by Do and Lee (2013), as described in equations (8) and (9).

$2(\text{R-COH}) + Pb^{2+} \rightarrow (\text{R-CO})_2Pb + 2H^+$ (8)

$2\text{R-COOH} + Pb^{2+} \rightarrow (\text{R-COO})_2Pb + 2H^+$ (9)

In addition to these mechanisms, the adsorption of Pb^{2+} likely occurred via hydrogen bonding mechanisms, as proposed by He et al. (2019) and illustrated in equations (10) and (11).

$\text{R-COH} + Pb(OH)^+ \rightarrow \text{R-COPb(OH)} + H^+$ (10)

$2(\text{R-COH}) + Pb(OH)_2 \rightarrow (\text{R-COH})_2Pb(OH)_2$ (11)

Based on the results from adsorption kinetics (Table 2) and adsorption thermodynamics (Table SM4), the pseudo second-order kinetic model provided a more accurate depiction of the adsorption behaviour for Pb^{2+} on Fe-Mn@BC. This suggests that the primary governing factor in the adsorption of Pb^{2+} on Fe-Mn@BC is chemical adsorption. Importantly, as chemisorption commonly occurs when ΔH is within the $20-200$ kJ/mol range, and the ΔH value for Fe-Mn@BC was determined to be 122.30 kJ/mol, it falls within this range. This confirms that chemical adsorption is the dominant adsorption process. This consistency agrees with the results obtained from the fitting of the pseudo second-order kinetic model. Proposed mechanisms for Pb^{2+} sorption onto Fe-Mn@BC are depicted in Fig. 6.

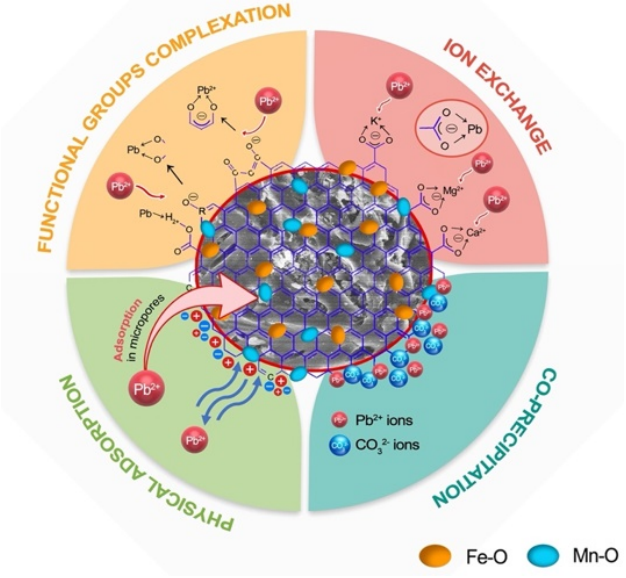

Figure 6. Potential mechanisms for the sorption of Pb^{+2} using Fe-Mn@BC.

4. Conclusion

The facile preparation of Fe-Mn modified biochar adsorbent was successfully achieved via the co-precipitation method. Following the modification process, higher surface area, and larger pore volume were observed, along with abundant oxygen functional groups such as -C-O/C=O and Fe-O/Mn-O. These enhancements contributed to a significant improvement in Pb^{2+} adsorption capacity. The optimal conditions for Pb^{2+} removal in this study were determined as follows: initial Pb^{2+} concentration of 50 mg/L, adsorbent amount of 0.01 g, adsorption time of 60 minutes, and adsorption temperature of 313 K. The q_{max} value for Pb^{2+} adsorption onto Fe-Mn modified biochar was determined to be 1164.95 mg/g, showcasing superior performance compared to both the original biochar (828.84 mg/g) and previous references. The adsorption behaviour of Pb^{2+} on Fe-Mn@BC was well-described by the pseudo second-order kinetic and Freundlich models. The dominant mechanism governing the adsorption of Pb^{2+} by Fe-Mn@BC was identified as chemical adsorption, taking place on a heterogeneous surface with a nonuniform distribution of heat of adsorption. Additionally, the adsorption process was determined to be spontaneous and endothermic. The controlling step in the adsorption rate was recognized as a combination of chemisorption and intraparticle diffusion, with external mass transfer exerting primary influence during the initial twenty minutes of the experiment. In conclusion, the iron/manganese binary oxide loaded on *Eichhornia crassipes* stem biochar demonstrates effective adsorption capabilities for Pb^{2+}, highlighting its potential as a promising adsorbent for the removal of Pb^{2+} from wastewater. Moving forward, future research should focus on investigating desorption mechanisms and developing strategies to enhance the practical applicability of Fe-Mn modified biochar adsorbent in water treatment processes.

Acknowledgment

The authors would like to thank the advanced technology laboratory of Can Tho University funded JICA for analysing the Pb^{2+}.

Funding

This study is funded in part by the Can Tho University, grant number T2023-38.

Authors contributions
The authors confirm the study conception and design: N. X. Loc, D. T. M. Phuong; data collection: L. H. Phong; analysis and interpretation of results: T. T. Bao, L. H. Phong, P. T. T. Tuyen; draft manuscript preparation: N. X. Loc, D. T. M. Phuong. The results were evaluated by all authors, and the final version of the manuscript was approved.

Availability of data and materials
The data that support the findings of this study are available from the corresponding author upon reasonable request.

Conflict of interests
The authors declare that they have no known competing financial interests or personal relationships that could have appeared to influence the work reported in this paper.

References

Akintola AT, Akinlabi ET, Masebinu SO (2020) Biochar as an adsorbent: a short overview. Valorization of biomass to value-added commodities: Current trends, challenges, and future prospects. *Springer,* https://doi.org/10.1007/978-3-030-38032-8-19

Bao D, Li Z, Tang R, Wan C, Zhang C, Tan X, Liu X (2021) Metal-modified sludge-based biochar enhance catalytic capacity: Characteristics and mechanism. *J Environ Manage* 284:112113. https://doi.org/10.1016/j.jenvman.2021.112113

Benettayeb A, Ghosh S, Usman M, Seihoub FZ, Sohoo I, Chia CH, Sillanpää M (2022) Some well-known alginate and chitosan modifications used in adsorption: A review. *Water* 14 (9): 1353. https://doi.org/10.3390/w14091353

Bopda A, Tchuifon DRT, Ndifor-Angwafor NG, Doungmo G, Gabche AS (2019) Non-linear equilibrium and kinetic study of the adsorption of 2, 4-dinitrophenol from aqueous solution using activated carbon derived from olives stones and cotton cake. *Afr J Environ Sci Technol* 13 (9): 365–380. https://doi.org/10.5897/AJEST2019.2717

Carneiro MT, Morais AIS, Carvalho Melo ALF de, Ferreira FJL, Santos FEP, Viana BC, Silva-Filho EC (2023) Biochar derived from water hyacinth biomass chemically activated for dye removal in aqueous solution. *Sustainability* 15 (19): 14578. https://doi.org/10.3390/su151914578

Chen C, Qiu M (2021) High efficiency removal of Pb (II) in aqueous solution by a biochar-supported nanoscale ferrous sulfide composite. *RSC Adv* 11 (2): 953–959. https://doi.org/10.1039/D0RA08055A

Chen L, Li F, Wei Y, Li G, Shen K, He HJ (2019) High cadmium adsorption on nanoscale zero-valent iron coated *Eichhornia crassipes* biochar. *Environ Chem Lett* 17:589–594. https://doi.org/10.1007/s10311-018-0811-y

Chen Z, Nan Z (2011) Controlling the polymorph and morphology of $CaCO_3$ crystals using surfactant mixtures. *J Colloid Interface Sci* 358 (2): 416–422. https://doi.org/10.1016/j.jcis.2011.02.062

Deb A, Das S, Debnath A (2023) Fabrication and characterization of organometallic nanocomposite for efficient abatement of dye laden wastewater: CCD optimization, adsorption mechanism, co-existing ions, and cost analysis. *Chem Phys Lett* 830:140820. https://doi.org/10.1016/j.cplett.2023.140820

Deng H, Zhang J, Huang R, Wang W, Meng M, Hu L, Gan W (2022) Adsorption of malachite green and Pb^{2+} by $KMnO_4$-modified biochar: Insights and mechanisms. *Sustainability* 14 (4): 2040. https://doi.org/10.3390/su14042040

Do XH, Lee BK (2013) Removal of Pb^{2+} using a biochar–alginate capsule in aqueous solution and capsule regeneration. *J Environ Manage* 131:375–382. https://doi.org/10.1016/j.jenvman.2013.09.045

Dong Y, Zeng W, Lin H, Yang Y (2022) Preparation of Fe_2O_3-coated vermiculite composite by hydrophobic agglomeration and its application in As/Cd co-contaminated soil. *Environ Technol* 43 (1): 83–94. https://doi.org/10.1080/09593330.2020.1777589

Dwivedi P, Narvi SS, Tewari RP, Tiwary D (2022) Nanobiotechnology for safe bioactive nanobiomaterials. *CRC Press*

Fan Y, Wang H, Deng L, Wang Y, Kang D, Li C, Chen H (2020) Enhanced adsorption of Pb (II) by nitrogen and phosphorus co-doped biochar derived from Camellia oleifera shells. *Environ Res* 191:110030. https://doi.org/10.1016/j.envres.2020.110030

Fang L, Li JS, Donatello S, Cheeseman CR, Poon CS, Tsang DC (2020) Use of Mg/Ca modified biochars to take up phosphorus from acid-extract of incinerated sewage sludge ash (ISSA) for fertilizer application. *J Clean Prod* 244:118853. https://doi.org/10.1016/j.jclepro.2019.118853

Ghorbani M, Seyedin O, Aghamohammadhassan M (2020) Adsorptive removal of lead (II) ion from water and wastewater media using carbon-based nanomaterials as unique sorbents: A review. *J Environ Manage* 254:109814. https://doi.org/10.1016/j.jenvman.2019.109814

Goswami M, Devi B, Baruah NP, Rabha S, Bharatwaj A, Sarma HP, Devi A (2024) Waste to wealth strategies or removal of Pb^{2+} ions from aqueous solution. *Inorg Chem Commun* 161:112097. https://doi.org/10.1016/j.inoche.2024.112097

Hashem MA, Hasan M, Momen MA, Payel S, Nur-A-Tomal MS (2020) Water hyacinth biochar for trivalent chromium adsorption from tannery wastewater. *Environ Sustain* 5:100022. https://doi.org/10.1016/j.indic.2020.100022

He Y, Wu P, Xiao W, Li G, Yi J, He Y, et al. (2019) Efficient removal of Pb (II) from aqueous solution by a novel ion imprinted magnetic biosorbent: Adsorption kinetics and mechanisms. *PloS one* 14 (3): e0213377. https://doi.org/10.1371/journal.pone.0213377

Hospodarova V, Singovszka E, Stevulova N (2018) Characterization of cellulosic fibers by FTIR spectroscopy for their further implementation to building materials. *Am J Anal Chem* 9 (6): 303–310. https://doi.org/10.4236/ajac.2018.96023

Idress H, Zaidi SZJ, Sabir A, Shafiq M, Khan RU, Harito C, Hassan S, Walsh FC (2021) Cellulose acetate based Complexation-NF membranes for the removal of Pb (II) from waste water. *Sci Rep* 11 (1): 1806. https://doi.org/10.s41598-020-80384-0

Jokar M, Mirghaffari N, Soleimani M, Jabbari M (2019) Preparation and characterization of novel bio ion exchanger from medicinal herb waste (chicory) for the removal of Pb^{2+} and Cd^{2+} from aqueous solutions. *J Water Process Eng* 28:88–99. https://doi.org/10.1016/j.jwpe.2019.01.007

Koyuncu DDE, Okur M (2021) Removal of AV 90 dye using ordered mesoporous carbon materials prepared via nanocasting of KIT-6: Adsorption isotherms, kinetics and thermodynamic analysis. *Sep Purif Technol* 257:117657. https://doi.org/10.1016/j.seppur.2020.117657

Li H, Chen Y, Long J, Li X, Jiang D, Zhang P, et al. (2017) Removal of thallium from aqueous solutions using Fe-Mn binary oxides. *J Hazard Mater* 338:296–305. https://doi.org/10.1016/j.jhazmat.2017.05.033

Lian W, Yang L, Joseph S, Shi W, Bian R, Zheng J, Li L, Shan S, Pan G (2020) Utilization of biochar produced from invasive plant species to efficiently adsorb Cd (II) and Pb (II). *Bioresour Technol* 317:124011. https://doi.org/10.1016/j.biortech.2020.124011

Liang J, Li X, Yu Z, Zeng G, Luo Y, Jiang L, et al. (2017) Amorphous MnO_2 modified biochar derived from aerobically composted swine manure for adsorption of Pb (II) and Cd (II). *ACS Sustain Chem Eng* 5 (6): 5049–5058. https://doi.org/10.1021/acssuschemeng.7b00434

Liang M, Xu S, Zhu Y, Chen X, Deng Z, Yan L, He H (2020) Preparation and characterization of Fe-Mn binary oxide/mulberry stem biochar composite adsorbent and adsorption of Cr (VI) from aqueous solution. *Int J Environ Res Public Health* 17 (3): 676. https://doi.org/10.3390/ijerph17030676

Lin L, Qiu W, Wang D, Huang Q, Song Z, Chau HW (2017) Arsenic removal in aqueous solution by a novel Fe-Mn modified biochar composite: characterization and mechanism. *Ecotoxicol Environ Saf* 144:514–521. https://doi.org/10.1016/j.ecoenv.2017.06.063

Liu C, Ye J, Lin Y, Wu J, Price GW, Burton D, Wang Y (2020) Removal of Cadmium (II) using water hyacinth (*Eichhornia crassipes*) biochar alginate beads in aqueous solutions. *Environ Pollut* 264:114785. https://doi.org/10.1016/j.envpol.2020.114785

Liu Q, Jiang S, Su X, Zhang X, Cao W, Xu Y (2021) Role of the biochar modified with $ZnCl_2$ and $FeCl_3$ on the electrochemical degradation of nitrobenzene. *Chemosphere* 275:129966. https://doi.org/10.1016/j.chemosphere.2021.129966

Liu Y, Guo J, Xiao Z, Peng D, Song K (2020b) Adsorption kinetics and isotherms of berberine by ZSM-5 molecular sieves from Cortex Phellodendron. *React Kinet Mech Catal* 129:491–504. https://doi.org/10.1007/s11144-019-01703-9

Liu Z, Xu Z, Xu L, Buyong F, Chay TC, Li Z, Cai Y, Hu B, Zhu Y, Wang X (2022) Modified biochar: synthesis and mechanism for removal of environmental heavy metals. *Carbon Res* 1 (1): 8. https://doi.org/10.1007/s44246-022-00007-3

Loc NX, Thanh TD, Phuong DTM (2023) Physicochemical properties of biochar produced from biodegradable domestic solid waste and sugarcane bagasse. *Int J Recycl Org Waste Agricul* 12 (3) https://doi.org/10.30486/ijrowa.2022.1954704.1429

Mongkollertlop S (2020) Investigation on adsorption behaviors of heavy metal ions (Cd^{2+}, Cr^{3+}, Hg^{2+} and Pb^{2+}) through low-cost/active manganese dioxide-modified magnetic biochar derived from palm kernel cake residue. *J Environ Chem Eng* 8 (6): 104467. https://doi.org/10.1016/j.jece.2020.104467

Narayanan M, Kandasamy G, Kandasamy S, Natarajan D, Devarayan K, Alsehli M, et al. (2021) Water hyacinth biochar and *Aspergillus niger* biomass amalgamation potential in removal of pollutants from polluted lake water. *J Environ Chem Eng* 9 (4): 105574. https://doi.org/10.1016/j.jece.2021.105574

Nasser MS, Abbas M, Trari M (2024) Understanding the rate-limiting step adsorption kinetics onto biomaterials for mechanism adsorption control. *Prog React Kinet Mech* 49:14686783241226858. https://doi.org/10.1177/14686783241226

Nguyen LX, Do PTM, Nguyen CH, Kose R, Okayama T, Pham TN, et al. (2018) Properties of biochars prepared from local biomass in the Mekong Delta, Vietnam. *Bioresour* 13 (4): 7325–7344.

Park Y, Liu S, Gardner T, Johnson D, Keeler A, Ortiz N, Rabah G, Ford E (2020) Biohybrid nanofibers containing manganese oxide–forming fungi for heavy metal removal from water. *J Eng Fiber Fabr J Eng* 15:1558925019898954. https://doi.org/10.1177/1558925019898954

Peng Z, Zhao H, Lyu H, Wang L, Huang H, Nan Q, Tang J (2018) UV modification of biochar for enhanced hexavalent chromium removal from aqueous solution. *Environ Sci Pollut Res* 25:10808–10819. https://doi.org/10.1007/s11356-018-1353-3

Phuong DTM, Loc NX, Miyanishi T (2019) Efficiency of dye adsorption by biochars produced from residues of two rice varieties, Japanese Koshihikari and Vietnamese IR50404. *Desalin Water Treat* 165:333–351. https://doi.org/10.5004/dwt.2019.24496

Qiu Y, Zhang Q, Li M, Fan Z, Sang W, Xie C, Niu D (2019) Adsorption of Cd (II) from aqueous solutions by modified biochars: Comparison of modification methods. *Water Air Soil Pollut* 230:1–11. https://doi.org/10.1007/s11270-019-4135-8

Qiu Y, Zhang Q, Wang Z, Gao B, Fan Z, Li M, Hao H, Wei X, Zhong M (2021) Degradation of anthraquinone dye reactive blue 19 using persulfate activated with Fe/Mn modified biochar: Radical/non-radical mechanisms and fixed-bed reactor study. *Sci Total Environ* 758:143584. https://doi.org/10.1016/j.scitotenv.2020.143584

Qu J, Che N, Niu G, Liu L, Li C, Liu Y (2023) Iron/manganese binary metal oxide-biochar nano-composites with high adsorption capacities of Cd^{2+}: Preparation and adsorption mechanisms. *J Water Process Eng* 51:103332. https://doi.org/10.1016/j.jwpe.2022.103332

Raj K, Das AP (2023) Lead pollution: Impact on environment and human health and approach for a sustainable solution. *Environ Toxicol Chem* 5:79–85. https://doi.org/10.1016/j.enceco.2023.02.001

Sadegh-Zadeh F, Seh-Bardan BJ (2013) Adsorption of As (III) and As (V) by Fe coated biochars and biochars produced from empty fruit bunch and rice husk. *J Environ Chem Eng* 1 (4): 981–988. https://doi.org/10.1016/j.jece.2013.08.009

Saha B, Gayen S, Debnath A (2023b) Sequestration of paracetamol from aqueous solution using zinc oxide/polypyrrole nanocomposite: Cost analysis, scale-Up design, and optimization of process parameters. *J Hazard Toxic Radioact Waste* 27 (4): 04023032. https://doi.org/10.1061/JHTRBP.HZENG-1213

Saha B, Shaji S, Debnath A (2023a) Fabrication of polyaniline based calcium ferrite nanocomposite and its application in sequestration of Victoria blue dye from wastewater. *J Dispers Sci Technol,* 1–15. https://doi.org/10.1080/01932691.2023.2273432

Saleh TA (2022) Surface science of adsorbents and nanoadsorbents: Properties and applications in environmental remediation. *Academic Press*

Sarkar S, Guibal E, Quignard F, SenGupta AK (2012) Polymer-supported metals and metal oxide nanoparticles: Synthesis, characterization, and applications. *J Nanopart Res* 14:1–24. https://doi.org/10.1007/s11051-011-0715-2

Sharma D, Chaudhari PK, Prajapati AK (2020) Removal of chromium (VI) and lead from electroplating effluent using electrocoagulation. *Sep Sci Technol* 55 (2): 321–331. https://doi.org/10.1080/01496395.2018.1563157

Sivaranjanee R, Kumar PS, Rangasamy G (2023) A critical review on biochar for environmental applications. *Carbon Lett* 33:1407–1432. https://doi.org/10.1007/s42823-023-00527-x

Suwunwong T, Danwittayakul P, Thanomsilp C, Siriwat P, Chantrapromma S, Phoungthong K (2021) The removal of Pb^{2+} ion by $MnFe_2O_4$/waste tea leaves biochar and mechanism of adsorption. *Mater Res Express* 8 (1): 015505. https://doi.org/10.1088/2053-1591/abd4b2

Tan G, Sun W, Xu Y, Wang H, Xu N (2016) Sorption of mercury (II) and atrazine by biochar, modified biochars and biochar based activated carbon in aqueous solution. *Bioresour Technol* 211:727–735. https://doi.org/10.1016/j.biortech.2016.03.147

Tan WT, Zhou H, Tang SF, Zeng P, Gu JF, Liao BH (2022) Enhancing Cd (II) adsorption on rice straw biochar by modification of iron and manganese oxides. *Environ Pollut* 300:118899. https://doi.org/10.1016/j.envpol.2022.118899

Tan Y, Yin X, Wang C, Sun H, Ma A, Zhang G, Wang N (2019) Sorption of cadmium onto Mg-Fe layered double hydroxide (LDH)-Kiwi branch biochar. *Environ Pollut Bioavailab* 31 (1): 189–197. https://doi.org/10.1080/26395940.2019.1604165

Tang SF, Zhou H, Tan WT, Huang JG, Zeng P, Gu JF, Liao BH (2022) Adsorption characteristics and mechanisms of Fe-Mn oxide modified biochar for Pb (II) in wastewater. *Int J Environ Res Public* 19 (14): 8420. https://doi.org/10.3390/ijerph19148420

Tran HN, You SJ, Hosseini-Bandegharaei A, Chao HP (2017) Mistakes and inconsistencies regarding adsorption of contaminants from aqueous solutions: A critical review. *Water Res* 120:88–116. https://doi.org/10.1016/j.watres.2017.04.014

Wang J, Guo X (2022) Rethinking of the intraparticle diffusion adsorption kinetics model: Interpretation, solving methods and applications. *Chemosphere* 309:136732. https://doi.org/10.1016/j.chemosphere.2022.136732

Wang J, Wang T, Zhu Q, Zhang S, Shi Q, Chovelon JM, Wang H (2021a) Preparation of a novel sludge-derived biochar by K_2FeO_4 conditioning to enhance the removal of Pb^{2+}. *Colloids Interface Sci Commun* 42:100417. https://doi.org/10.1016/j.colcom.2021.100417

Wang J, Zhao M, Zhang J, Zhao B, Lu X, Wei H (2021) Characterization and utilization of biochars derived from five invasive plant species *Bidens pilosa L.*, Praxelis clematidea, Ipomoea cairica, Mikania micrantha and Lantana camara L. for Cd^{2+} and Cu^{2+} removal. *J Environ Manage* 280:111746. https://doi.org/10.1016/j.jenvman.2020.111746

Wang Q, Wang Y, Yang Z, Han W, Yuan L, Zhang L, et al. (2022a) Efficient removal of Pb (II) and Cd (II) from aqueous solutions by mango seed biosorbent. *Chem Eng J Adv* 11:100295. https://doi.org/10.1016/j.ceja.2022.100295

Wang X, Guo X, Li T, Zhu J, Pang J, Xu J, Wang J, Huang X, Gao J, Wang L (2022b) Study on adsorption characteristics of heavy metal Cd^{2+} by biochar obtained from water hyacinth. *Pol J Environ Stud* 31 (3) https://doi.org/10.15244/pjoes/141045

Wang YY, Ji HY, Lu HH, Liu YX, Yang RQ, He LL, Yang SM (2018) Simultaneous removal of Sb (III) and Cd (II) in water by adsorption onto a $MnFe_2O_4$–biochar nanocomposite. *RSC Adv* 8 (6): 3264–3273. https://doi.org/10.1039/C7RA13151H

Xiang J, Lin Q, Cheng S, Guo J, Yao X, Liu Q, Yin G, Liu D (2018) Enhanced adsorption of Cd (II) from aqueous solution by a magnesium oxide–rice husk biochar composite. *Environ Sci Pollut Res* 25:14032–14042. https://doi.org/10.1007/s11356-018-1594-1

Xu Z, Gu S, Rana D, Matsuura T, Lan CQ (2021) Chemical precipitation enabled UF and MF filtration for lead removal. *J Water Proc Eng* 41:101987. https://doi.org/10.1016/j.jwpe.2021.101987

Yin G, Song X, Tao L, Sarkar B, Sarmah AK, Zhang W, Lin Q, Xiao R, Liu Q, Wang H (2020) Novel Fe-Mn binary oxide-biochar as an adsorbent for removing Cd (II) from aqueous solutions. *J Chem Eng* 389:124465. https://doi.org/10.1016/j.cej.2020.124465

Zhang A, Li X, Xing J, Xu G (2020a) Adsorption of potentially toxic elements in water by modified biochar: A review. *J Environ Chem Eng* 8 (4): 104196. https://doi.org/10.1016/j.jece.2020.104196

Zhang H, Xu F, Xue J, Chen S, Wang J, Yang Y (2020b) Enhanced removal of heavy metal ions from aqueous solution using manganese dioxide-loaded biochar: Behavior and mechanism. *Sci Rep* 10 (1): 067. https://doi.org/10.1038/s41598-020-63000-z

Zhang L, Liu X, Huang X, Wang W, Sun P, Li Y (2019) Adsorption of Pb^{2+} from aqueous solutions using Fe–Mn binary oxides-loaded biochar: Kinetics, isotherm and thermodynamic studies. *Environ Technol* 40 (14): 1853–1861. https://doi.org/10.1080/09593330.2018.1432693

Zhao T, Ma X, Cai H, Ma Z, Liang H (2020) Study on the adsorption of $CuFe_2O_4$-loaded corncob biochar for Pb (II). *Molecules* 25 (15): 3456. https://doi.org/10.3390/molecules25153456

Zheng Q, Tu S, Hou J, Ni C, Wang M, Ren L, et al. (2021) Insights into the underlying mechanisms of stability working for As (III) removal by Fe-Mn binary oxide as a highly efficient adsorbent. *Water Res* 203:117558. https://doi.org/10.1016/j.watres.2021.117558

Zhou Q, Liao B, Lin L, Qiu W, Song Z (2018) Adsorption of Cu (II) and Cd (II) from aqueous solutions by ferromanganese binary oxide–biochar composites. *Sci Total Environ* 615:115–122. https://doi.org/10.1016/j.scitotenv.2017.09.220

Zhou R, Zhang M, Zhou J, Wang J (2019) Optimization of biochar preparation from the stem of *Eichhornia crassipes* using response surface methodology on adsorption of Cd^{2+}. *Sci Rep* 9 (1): 17538. https://doi.org/10.1038/s41598-019-54105-1

Zhu S, Zhao J, Zhao N, Yang X, Chen C, Shang J (2020) Goethite modified biochar as a multifunctional amendment for cationic Cd (II), anionic as (III), roxarsone, and phosphorus in soil and water. *J Clean Prod* 247:119579. https://doi.org/10.1016/j.jclepro.2019.119579

Supplementary material

Supplementary Tables

Table SM1. Adsorption kinetic models.

Kinetic	Functional form	Linear form	Plot	Parameters and Constants
Pseudo-second order	$\frac{dq_t}{dt} = k_2(q_e - q_t)^2$	$\frac{t}{q_t} = \frac{1}{k_2 q_e^2} + \frac{1}{q_e}t$	$\log \frac{t}{q_t}$ versus t	q_e: Equilibrium adsorption capacity (mg/g); q_t: Time adsorption capacity (mg/g); t: the contact time (min); k_2: Second-order rate coefficient (g/mg.min)
Elovich equation	$\frac{dq_t}{dt} = \alpha \exp(-\beta q_t)$	$q_t = \frac{1}{\beta}\ln(\alpha\beta) + \frac{1}{\beta}\ln t$	q_t versus $\ln t$	q_t: Time adsorption capacity (mg/g) t: the contact time (min); α: initial adsorption rate (mg/g.min); β: related to the extended of surface coverage and activation energy for chemisorption (g/mg).
Intraparticle Diffusion	$q_t = k_p t^{1/2} + \mathrm{C}$	$q_t = k_p t^{1/2} + \mathrm{C}$	q_t versus $t^{1/2}$	q_t: Time adsorption capacity (mg/g) k_p: the intra-particle diffusion rate constant (mg/g.min$^{1/2}$); t: the contact time (min); C: the constant related to the thickness of the boundary layer (mg/g).

Table SM2. Adsorption isotherm models.

Isotherm	Functional form	Linear form	Plot	Parameters and Constants
Langmuir	$q_e = \frac{q_m \mathrm{K}_L \mathrm{C}_e}{1+\mathrm{K}_L \mathrm{C}_e}$	$\frac{\mathrm{C}_e}{q_e} = \frac{1}{\mathrm{K}_L q_m} + \frac{\mathrm{C}_e}{q_m}$	$\frac{\mathrm{C}_e}{q_e}$ versus C_e	q_e: Adsorption capacity (mg/g); q_m: the maximum adsorption capacity (mg/g); C_e: Equilibrium concentration of the adsorbate (mg/L); K_L: the Langmuir adsorption constant (L/mg).
Freundlich	$q_e = \mathrm{K}_F \mathrm{C}_q^{1/\mathrm{n}}$	$\log q_e = \log \mathrm{K}_F + \frac{1}{\mathrm{n}} \log \mathrm{C}_e$	$\log q_e$ versus $\log \mathrm{C}_e$	q_e: Adsorption capacity (mg/g); C_e: Equilibrium concentration of the adsorbate (mg/L); K_F: the sorption affinity, (mg/kg)/(mg/L)$^{\mathrm{n}}$; 1/n: the nonlinearity index (unitless).
Temkin	$q_e = \frac{RT}{b}\ln(\mathrm{K}_T \mathrm{C}_e)$	$q_e = \frac{RT}{b}\ln \mathrm{K}_T + \frac{RT}{b}\ln \mathrm{C}$	q_e versus $\ln \mathrm{C}_e$	q_e: Adsorption capacity (mg/g); C_e: Equilibrium concentration of the adsorbate (mg/L); K_T: Equilibrium association constant (L/mg); b: Variation of the adsorption energy (J/mol); R: gas constant (8.314 J/mol.K); T: The absolute temperature in Kelvin (273 + °C).

Table SM3. Intra-particle diffusion parameters of Pb2+ adsorption.

Material	Intra-particle diffusion								
	Stage I (t: 1 – 20 min)			Stage II (t: 30 – 90 min)			Stage III (t > 120 min)		
	C_1 mg/g	k_{p1} mg/g.min$^{1/2}$	R^2 mg/g	C_2 mg/g.min$^{1/2}$	k_{p2} mg/g	R^2 mg/g.min$^{1/2}$	C_3	k_{p3} R^2	
BC	171.82	10.26	0.80	206.31	1.89	0.90	222.37	0.11	0.89
Fe-Mn@BC	223.63	7.37	0.77	250.03	0.94	0.86	257.93	0.05	0.99

Table SM4. Thermodynamic parameters of Pb^{2+} adsorption on BC and Fe-Mn@BC at different temperatures.

Material	T (K)	ΔG KJ/mol	ΔH KJ/mol	ΔS KJ/mol.K	R^2
BC	303	-7.99	62.05	0.231	1
	308	-9.15			
	313	-10.30			
Fe-Mn@BC	303	-9.32	122.30	0.434	0.9716
	308	-10.91			
	313	-13.67			

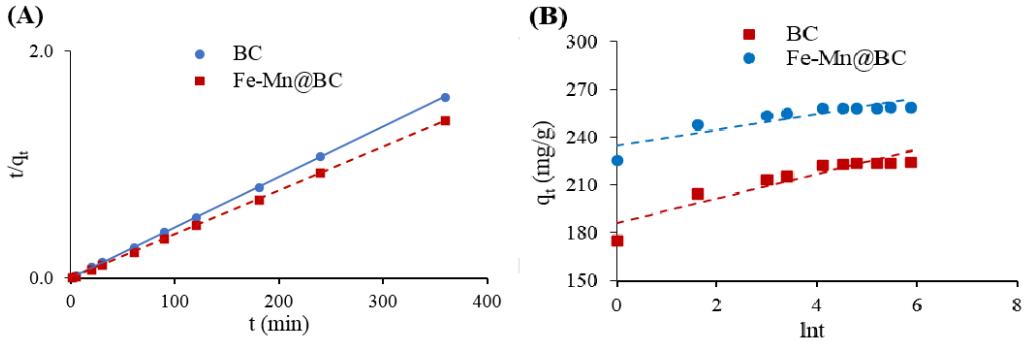

Figure SM1. Linearized pseudo second-order (A) and Elovich (B) kinetics for adsorption of Pb^{2+} onto BC and Fe-Mn@BC

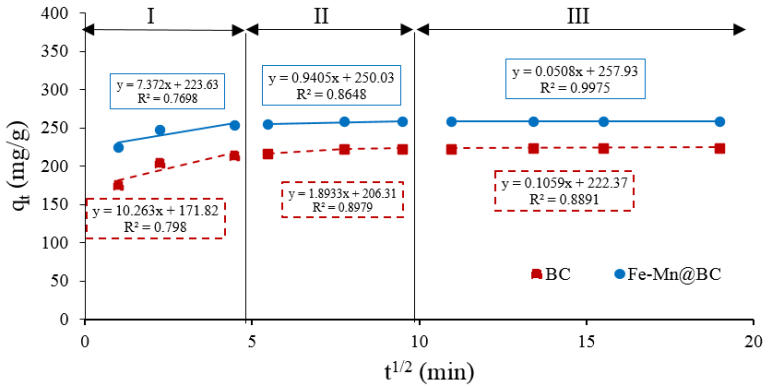

Figure SM2. Intra-particle diffusion kinetic model of BC and Fe-Mn@BC.

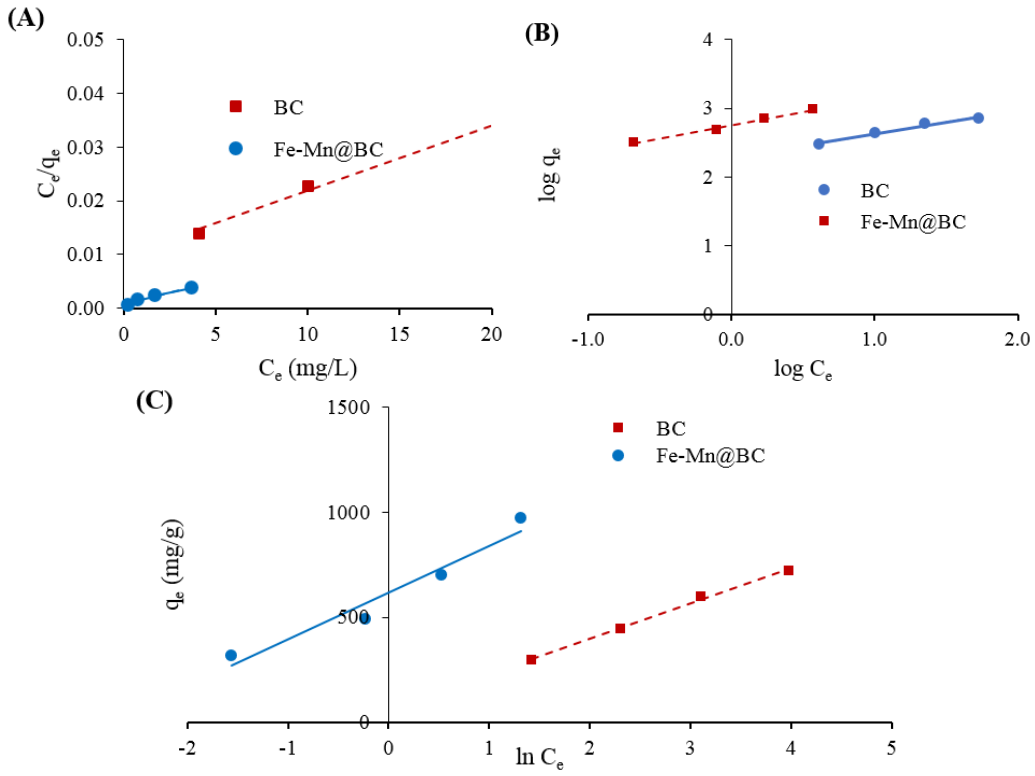

Figure SM3. Linearized Langmuir (A), Freundlich (B), and Temkin (C) isotherms for adsorption of Pb^{2+} onto BC and Fe-Mn@BC